Distal Proprioceptive Sensor for Motion Feedback in Endoscope-Based Modular Robotic Systems*

Joshua Gafford[1], Hiroyuki Aihara[2], Christopher Thompson[2], Robert Wood[3], and Conor Walsh[3]

***Abstract*—Modular robotic systems that integrate distally with commercially-available endoscopic equipment have the potential to improve the standard-of-care in therapeutic endoscopy by granting clinicians with capabilities not present in commercial tools, such as precision dexterity and feedback sensing. With the desire to integrate both sensing and actuation distally for closed-loop position control in fully-deployable, endoscope-based robotic modules, commercial sensor and actuator options that acquiesce to the strict form-factor requirements are sparse or nonexistent. Herein we describe a proprioceptive angle sensor for potential closed-loop position control applications in distal robotic modules. Fabricated monolithically using printed-circuit MEMS, the sensor employs a kinematic linkage and the principle of light intensity modulation to sense the angle of articulation with a high degree of fidelity. On-board temperature and environmental irradiance measurements, coupled with linear regression techniques, provide robust angle measurements that are insensitive to environmental disturbances. The sensor is capable of measuring ±45 degrees of articulation with an RMS error of 0.98 degrees. An *ex vivo* demonstration shows that the sensor can give real-time proprioceptive feedback when coupled with an actuator module, opening up the possibility of fully-distal closed-loop control.**

***Index Terms*—Medical Robots and Systems, Flexible Robots, Mechanism Design**

I. Introduction

THE desire to provide therapeutic treatment to remote or confined locations inside the body through natural orifices has driven innovation in flexible robotic and endoscopic systems capable of navigating circuitous anatomy and interacting with tissue [1]–[5]. Further, increasing interest in removing cancerous tissue from within the gastrointestinal (GI) tract endoscopically, as in endoscopic submucosal dissection, further motivates the development of advanced robotic endoscopic systems [6]. Due to the strict form factor requirements imposed by intraluminal navigation, integrating sensors and actuators distally remains a significant challenge. As such, many systems rely on proximal actuation schemes and sensing modalities or image guidance to close the loop.

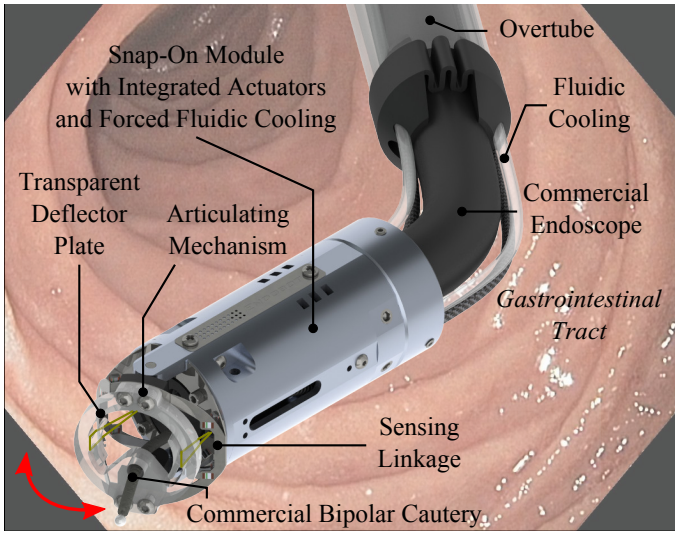

Fig. 1: Rendering of a distally-mounted robotic endoscopic module with an integrated sensing linkage for proprioceptive feedback.

In our previous work, we developed an endoscope-mounted modular robotic system with integrated shape-memory alloy (SMA) actuation, and demonstrated that such a device can enable active control of otherwise passive flexible endoscope tools for enhanced dexterity *in vivo* [7]. Such an approach could enable low-cost, disposable systems that reduce sterilization requirements and fill the niche that exists between manual tools already on the market and highly-dexterous, fully robotic endoscopic systems that are becoming clinically viable. However, the nonlinear and hysteretic behavior of the SMA actuation methodology can make open-loop control a challenge. As such, it is highly desirable to integrate distal sensing to provide real-time feedback for loop closure, shown conceptually in Fig. 1.

A. The Need for Feedback Control

Endoscopic Submucosal Dissection (ESD), a promising technique used to remove mid-size cancerous lesions from the submucosal space of the gastrointestinal tract *en bloc*, consists of several subtasks that are cognitively burdensome to the endoscopist due to the remote location of the lesions inside the GI tract and the unintuitive mapping between the endoscope input space and resulting tip motion in task space.

Manuscript received: February 14, 2017; Revised June 2, 2017; Accepted July 10, 2017.

This paper was recommended for publication by Editor Ken Masamune upon evaluation of the Associate Editor and Reviewers' comments. *This material based on work supported by Defense Advanced Research Projects Agency (DARPA), A2P (Grant No. FA8650-15-C-7548). This work was also partially funded by the Wyss Institute for Biologically Inspired Engineering and the John A. Paulson School of Engineering and Applied Sciences at Harvard University. In addition, the prototypes were enabled by equipment supported by the ARO DURIP program (Award No. W911NF-13-1-0311).

[1]Joshua Gafford (corresponding author) is with the John A. Paulson School of Engineering and Applied Sciences, Harvard University, Cambridge, MA 02138, USA (jgafford@seas.harvard.edu)

[2]Hiroyuki Aihara and Christopher Thompson are with Brigham and Women's Hospital, Boston, MA 02115, USA (haihara, ccthompson@bwh.harvard.edu)

[3]Robert Wood and Conor Walsh are with the John A. Paulson School of Engineering and Applied Sciences and the Wyss Institute for Biologically-Inspired Engineering, Cambridge, MA 02138, USA (rjwood, walsh@seas.harvard.edu)

Digital Object Identifier (DOI): see top of this page.

This article has been accepted for publication in a future issue of this journal, but has not been fully edited. Content may change prior to final publication. Citation information: DOI 10.1109/LRA.2017.2737042, IEEE Robotics and Automation Letters

The subtask that requires the most dexterity involves making a series of lateral incisions underneath the lesion using side-cutting electrosurgical tools to 'lift off' the lesion from the submucosal space. This maneuver manifests as a coupled motion consisting of a lateral sweeping motion to perform cutting and a slow retraction of the tool to provide tissue countertraction. Our desire is to potentially automate low-level tasks such as the lateral sweeping motion while relegating master control over the endoscope's gross motion to the endoscopist in a collaborative control methodology, thereby reducing the cognitive loading on the practitioner.

From a technical perspective, the need for angle feedback sensing for precision control in an antagonistic SMA configuration is apparent if we consider the complex thermomechanical behavior of the actuators [7]. For example, consider an open-loop control scenario where the clinician commands a positive articulation angle, thereby passing a current to one of the actuators. When the command is removed, the SMA may continue to heat up, causing further motion which is undesirable for precision control. In a closed-loop application, the sensor would detect this deviation from the setpoint, and subsequently flush the previously active actuator while heating the bias actuator to maintain the desired angle. In addition, as the flexible electrosurgical tool adds an uncertain elastic load in parallel to the antagonistic configuration scheme, a lack of position control could produce undesired motion when the control signal is removed and the tool stiffness overcomes the stiffness of the bias actuator, causing springback of the deflection plate which a position controller would otherwise compensate for. As such, we would like to demonstrate the proposed sensor's utility for real-time angle feedback for potential closed-loop applications.

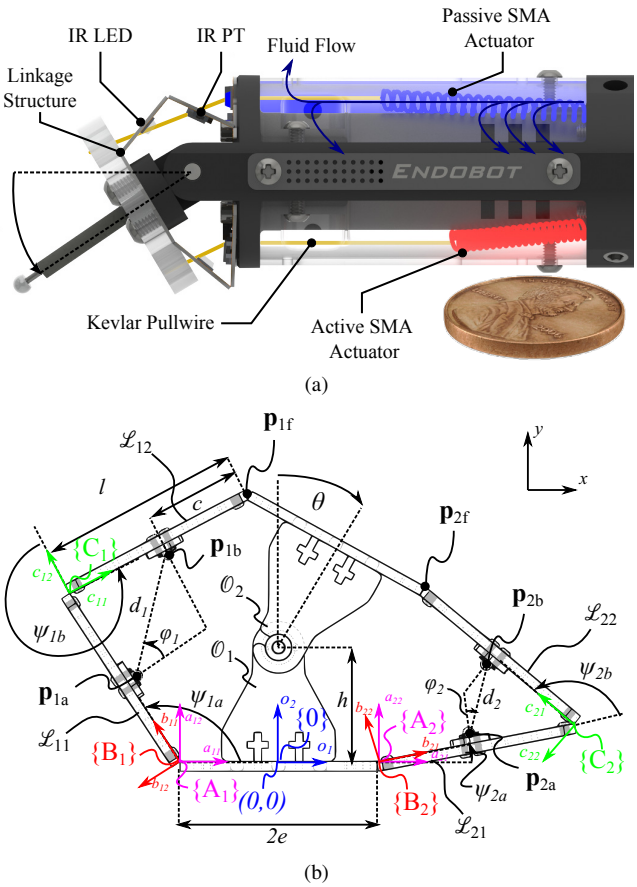

Fig. 2: *(a)* Illustration of the coupling between the sensor linkage and the antagonistic SMA actuation modality (with transparent covers to show actuator displacement), *(b)* kinematic illustration of the sensor linkage given a positive articulation angle θ.

B. Contribution

Integrating robust, high-range proprioceptive sensing modalities distally remains a challenge that conventional approaches to manufacturing are ill-suited for. The strict form-factor requirements, specifically the requirement for an unobstructed bore through which the commercial endoscope passes, precludes the use of off-the-shelf sensor modalities. The motivation of this work is to develop a high-fidelity, high-range proprioceptive angular sensor to detect articulation in a distally-mounted robotic module for endoscopy. A secondary motivation is 'mechanical transparency', in that the sensor adds little to no additional stiffness to the system to maximize the net force generated by the actuators. As strain-based sensing modalities implicitly rely on the elastic deformation of a continuum structure to sense deflection which invariably adds stiffness to the overall system, this approach was quickly discarded [8]. Capacitance-based sensing methodologies are not well suited for high-stroke applications and are highly susceptible to stray capacitances. A desire for low-cost, deployability and modularity rules out electromagnetic and fiber-based sensing modalities (FBG, Fabry-Perot) which typically require expensive interrogation equipment and introduce a necessary optical coupling between the distal end of the device and a proximal illumination and collection source [9], [10].

In our previous work, we have demonstrated the use of discrete emitter-detector (E/D) pairs and the principle of light-intensity modulation (LIM) to sense forces and displacements [11]. In this work, we explore monolithic fabrication techniques to develop an angular proprioceptive sensor within the context of distal robotic modules for endoscopy capable of actively articulating otherwise passive flexible endoscopic tools. By employing a kinematic linkage and the principle of LIM, articulation within the structure generated by on-board actuators directly translates to relative angular and linear displacement between emitter-detector pairs (as shown in Fig. 2 (a)) to produce a differential signal that can be used for position feedback and closed-loop control. The methodologies presented in this work are generalizable to discrete shape sensing in continuum robotics.

Section II presents a derivation of both kinematic and opto-electronic models used to predict sensor linkage performance. In Section III, we validate previously-derived analytical models with a 10× experimental model to prove feasibility of the concept. Section IV presents the fabrication of the to-scale sensor linkage. Section V discusses preliminary characterization results, as well as an integrated demonstration where the sensor gives real-time proprioceptive feedback in an endoscope-based robotic module during *ex vivo* ESD. Conclusions and areas of future work are discussed in Section VI.

This article has been accepted for publication in a future issue of this journal, but has not been fully edited. Content may change prior to final publication. Citation information: DOI 10.1109/LRA.2017.2737042, IEEE Robotics and Automation Letters

II. Kinematic Linkage Design and Modeling

The linkage design employs two coupled 4-bar linkages and their resulting kinematics transform an input angle θ into a relative misalignment and displacement between two emitter-detector pairs situated on symmetric but opposite sides of the system, creating a differential signal to reject common-mode noise. The following section presents a complete derivation of the analytical model used to size the kinematic linkage and assess the performance of different emitter-detector pairs.

A. Kinematics Model

Consider the schematic shown in Fig. 2 (b). An angular displacement θ is applied to input link $\mathcal{O}_2$ with respect to ground link $\mathcal{O}_1$ by the actuators [7]. Kinematics dictate the transformation between the input angle θ and relative output angles ψ between output links $\mathcal{L}$, upon which optical emitter-detector pairs are placed in opposing configurations.

Ultimately we would like a model that, for a given input angle θ, generates output voltages from the two phototransistors in the linkage. As such, we must solve for the kinematics of the system, and use resulting relative linear and angular displacements ($d_{1,2}$ and $\phi_{1,2}$, respectively) in an optoelectronics model that describes the incident irradiance attenuation factors due to displacement and misalignment, ultimately outputting the current drained by each phototransistor (and, subsequently, the voltage given a suitable signal conditioning model).

Henceforth, we define linkage k as the subset of all points that belong to their respective links ($\mathbf{p} \in \{L_{k1} \rightarrow L_{k2}\}$). We define points as $\mathbf{p}_{kj}^{\{m_k\}}$ where k is the linkage to which the point belongs (1 or 2 according to Fig. 2 (b)), j is a functional identifier (a, b, or f), and $\{m_k\}$ is the coordinate frame of reference (which is implicitly assigned to linkage k).

For rigid-body transformations, it is convenient to use homogeneous transformation matrices (HTM) to express positions and orientations in a local frame with respect to the inertial frame. For convenience, we define the following two-dimensional homogeneous transformation matrix (HTM):

$$\mathbf{H}(\alpha, \delta_x, \delta_y) = \begin{bmatrix} \cos(\alpha) & -\sin(\alpha) & \delta_x \\ \sin(\alpha) & \cos(\alpha) & \delta_y \\ 0 & 0 & 1 \end{bmatrix} \tag{1}$$

where α is the angle of rotation about the $z-$axis, and δ_x and δ_y are translations in x and y, respectively. We can re-express the transformation $\mathbf{p}_{1f}^{\{C\}\rightarrow\{O\}}$ as:

$$[\mathbf{p}_{1f}^{\{O\}} \quad 1]^T = \mathbf{H}(0, -e, 0)\mathbf{H}(\psi_{1a}, 0, 0)\mathbf{H}(\psi_{1b}, l, 0)[\mathbf{p}_{1f}^{\{C_1\}} \quad 1]^T \tag{2}$$

where geometric parameters (e, ψ and l) are as defined in Fig. 2 (vectors are padded so the algebra works out).

Although the forward kinematics are trivial to compute with HTMs given that we know linkage angles (i.e. given ψ, solve for θ), we are actually interested in solving the inverse problem (i.e. given θ, solve for ψ). We use the observation that linkages $\mathcal{L}_1$ and $\mathcal{L}_2$ are simply planar two-degree-of freedom revolute (RR) linkages with end-effector positions $\mathbf{p}_{1f}^{\{A_1\}}$ and $\mathbf{p}_{2f}^{\{A_2\}}$ expressed in the inertial frames $\{A_k\}$ assigned to each respective linkage. Given an input angle θ, we can use forward kinematics to express these points in the global inertial frame $\{O\}$:

$$[\mathbf{p}_{\bullet f}^{\{O\}} \quad 1]^T = \mathbf{H}(\theta, 0, h)[(-1)^\bullet e \quad h \quad 1]^T \tag{3}$$

Here we introduce $\bullet \in \{1, 2\}$ to denote the distinction between $\mathcal{L}_1$ and $\mathcal{L}_2$. To simplify subsequent algebra, we can express these points in each linkage's inertial frame:

$$[\mathbf{p}_{\bullet f}^{\{A_\bullet\}} \quad 1]^T = \mathbf{H}(0, -(-1)^\bullet e, 0)[\mathbf{p}_{\bullet f}^{\{O\}} \quad 1]^T \tag{4}$$

Implementing the law of cosines, we can algebraically solve for intermediate angles $\psi_{\bullet a}$ and $\psi_{\bullet b}$ as follows:

$$\psi_{\bullet b} = (-1)^\bullet \cos^{-1}\left(\frac{||\mathbf{p}_{\bullet f}^{\{A_\bullet\}}||^2 - 2l^2}{2l^2}\right) \tag{5}$$

$$\begin{aligned} \psi_{\bullet a} = &\tan^{-1}\left(\frac{\mathbf{p}_{\bullet f}^{\{A_\bullet\}}(2)}{\mathbf{p}_{\bullet f}^{\{A_\bullet\}}(1)}\right) \\ &- (-1)^\bullet \cos^{-1}\left(\frac{||\mathbf{p}_{\bullet f}^{\{A_\bullet\}}||^2}{2l||\mathbf{p}_{\bullet f}^{\{A_\bullet\}}||}\right) \end{aligned} \tag{6}$$

where $||\mathbf{x}||$ is the Euclidean norm of $\mathbf{x}$. Note that linkage 1 is the redundant ('elbow up') solution, hence the addition of the $(-1)^\bullet$ term which changes sign depending on the linkage being considered. The angular misalignment $\phi_\bullet$ can be expressed as:

$$\phi_\bullet = (-1)^\bullet \frac{\pi - \psi_{\bullet b}}{2} \tag{7}$$

Finally, we can express the coordinates of emitter $\mathbf{p}_{\bullet a\{O\}}$ and detector $\mathbf{p}_{\bullet b\{O\}}$ as:

$$\mathbf{p}_{\bullet a}^{\{O\}} = \mathbf{H}(\psi_{\bullet a}, (-1)^\bullet e, 0) \cdot \begin{bmatrix} c & 0 & 1 \end{bmatrix}^T \tag{8}$$

$$\mathbf{p}_{\bullet b}^{\{O\}} = \mathbf{H}(\psi_{\bullet a}, (-1)^\bullet e, 0) \cdot \mathbf{H}(\psi_{\bullet b}, l, 0) \cdot \begin{bmatrix} l - c & 0 & 1 \end{bmatrix}^T \tag{9}$$

The Euclidean distance separating emitter from detector is given by:

$$d_\bullet = ||\mathbf{p}_{\bullet b}^{\{O\}} - \mathbf{p}_{\bullet a}^{\{O\}}|| \tag{10}$$

B. Optoelectronics Model

The kinematics of the system manifest as attenuation factors in the optoelectronics model. The basis is a simple point-source model described more thoroughly in [12], where the irradiance falls off with the square of the distance from the LED. The misalignment attenuation factor for the LED is adequately modeled by an inverse sigmoidal function with fit parameters α as given by the following:

$$\eta_{\bullet LED} = \frac{\alpha_1}{1 + \exp(\alpha_2 - \alpha_3 \phi_\bullet)} \tag{11}$$

This article has been accepted for publication in a future issue of this journal, but has not been fully edited. Content may change prior to final publication. Citation information: DOI 10.1109/LRA.2017.2737042, IEEE Robotics and Automation Letters

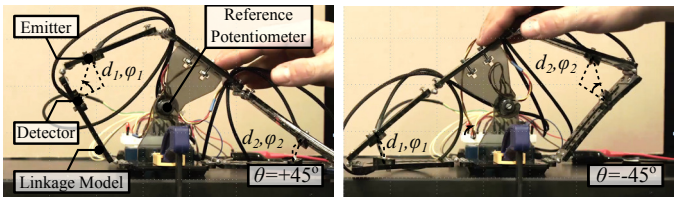

Fig. 3: Experiments with a 10× scale prototype, shown at extremes of travel.

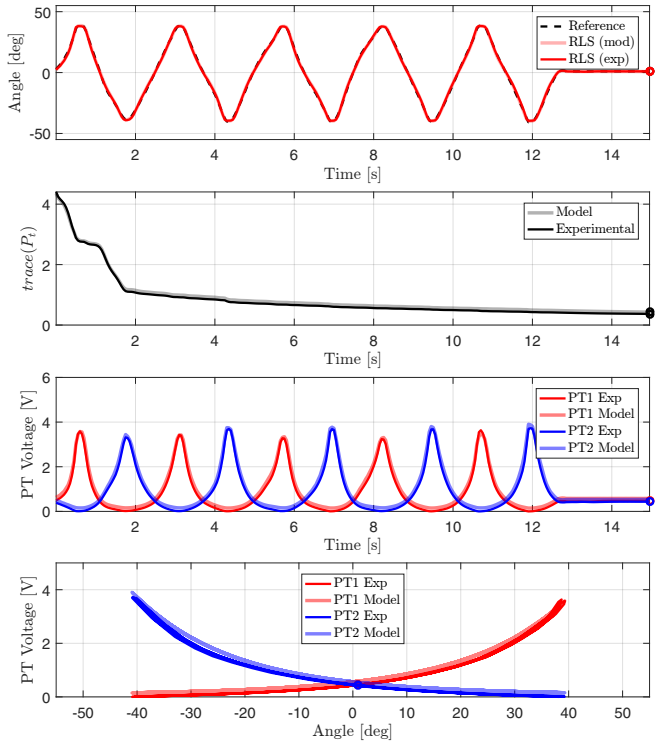

Fig. 4: Comparison of analytical and experimental results with the 10× scale model: *(from top)* RLS estimated angle $\hat{\theta}$ (analytical and experimental) compared to the actual angle θ vs. time, trace of the RLS covariance matrix P_t vs. time (analytical and experimental) provided as an objective measure of estimator convergence, phototransistor output voltage vs. time (analytical and experimental), phototransistor output voltage vs. input angle θ (analytical and experimental).

The misalignment attenuation factor for the PT is similarly described with fit parameters β:

$$\eta_{\bullet PT} = \frac{\beta_1}{1 + \exp\left(\beta_2 - \beta_3 \phi_\bullet\right)} \tag{12}$$

Finally, we can express the voltage generated by the phototransistor by the following:

$$V_{PT} = R_{PT}\eta_{\bullet PT}\eta_{\bullet LED}\left(\frac{\gamma_1 \Phi}{4\pi d_\bullet^2} + \gamma_2\right) \tag{13}$$

where R_{PT} is the resistance value used to convert the collector current into a voltage, γ are curve fit parameters and Φ is the radiant intensity generated by the LED.

III. Experiments with a Scale Model

To validate the previously-derived analytical model, a 10× scaled-up version of the PCMEMS sensor kinematic structure was built out of acrylic, as shown in Fig. 3. A potentiometer mounted at the center of rotation of the input linkage provides a ground-truth measurement of the input angle θ. The output links in the kinematic linkage have an array of mounting holes, allowing for arbitrary selection of the emitter-detector spatial location within the structure.

The goal of this scaled-up prototype is three-fold: (1) demonstrate feasibility of leveraging both displacement and misalignment within optoelectronic emitter-detector pairs to sense angular displacement, (2) validate previously-derived kinematics and optoelectronics models, and (3) assess the performance of linear regression models (with both linear and nonlinear feature spaces) on emitter-detector signals and the fidelity with which they approximate the true input angle.

A dynamic input was provided to the input link over the full range of motion (roughly ± 45 degrees). Meanwhile, potentiometer and phototransistor voltages were captured through NI LabView at a rate of 1 kHz. Data were post-processed in MATLAB. A recursive least-squares (RLS) algorithm with a quadratic feature space was implemented to estimate the input angle based on the E/D pair readings.

Example results are plotted in Fig. 4. The top plot shows the actual angle θ compared to estimates $\hat{\theta}_{mod}$ and $\hat{\theta}_{exp}$ which are estimated in real time using RLS. The second plot shows the trace of the covariance matrix P_t used in RLS, which provides a quantitative measure of estimator convergence. The third and fourth plots show the raw phototransistor output voltages (from both model and experiment) plotted against time and input angle, respectively. We observe that the experimental and analytical results are nearly identical, speaking to the fidelity of the theoretical model. In addition, the use of a quadratic feature space yields an exemplary estimate of the actual input angle and the RMS error is less than 1 degree.

IV. To-Scale Prototype Design and Fabrication

The 10× scale experimental model demonstrated concept feasibility in addition to validating the previously-derived analytical model. To fabricate the sensor linkage at the scale appropriate for distal implementation in endoscopy, we exploit alternative manufacturing techniques as described in the following section.

A. PCMEMS Fabrication

The at-scale prototype was fabricated using printed-circuit MEMS (PCMEMS). The laminate consists of seven layers of material: two layers of 125 μm thick 304 stainless steel, one layer of 50 μm thick Kapton polyimide, three layers of 25 μm FR0100 adhesive (duPont), and one layer of 25 μm thick Kapton with an 18 μm thick Copper cladding. The typical steps of this manufacturing process are more thoroughly described in [13]. The layers are individually machined in a diode-pumped solid-state (DPSS) laser and laminated together using heat and pressure (1). Release cuts are made in the DPSS laser (2) and the linkages are freed from their surrounding alignment scaffold. The top layer is a flexible circuit layer containing traces and land patterns for sensors and passive components which are soldered using reflow techniques (3). Finally, the

This article has been accepted for publication in a future issue of this journal, but has not been fully edited. Content may change prior to final publication. Citation information: DOI 10.1109/LRA.2017.2737042, IEEE Robotics and Automation Letters

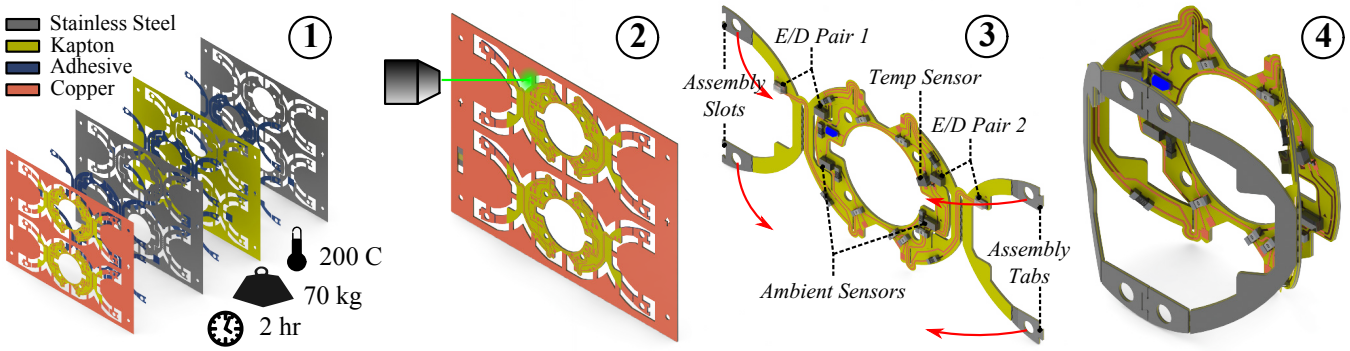

Fig. 5: Printed-circuit MEMS fabrication of the at-scale sensor linkage: (1) lamination of individually laser-machined material layers, (2) release cuts to free sensor linkage from alignment scaffold, (3) pick-and-placement of electronic components for reflow soldering, (4) tab-and-slot guided manual assembly.

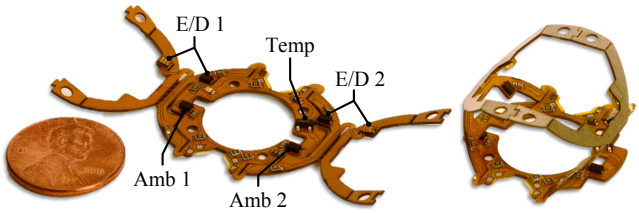

Fig. 6: To-scale sensor linkages shown both pre- and post-assembly with a US penny for scale.

linkage is manually assembled by out-of-plane folding and tab-and-slot assembly (4). This process is shown in Fig. 5. After component placement, the sensor is coated with a thin layer of silicone-based conformal coating to electrically isolate components and traces from fluidic environments. Photographs of the sensor linkage both pre- and post-assembly are shown in Fig. 6.

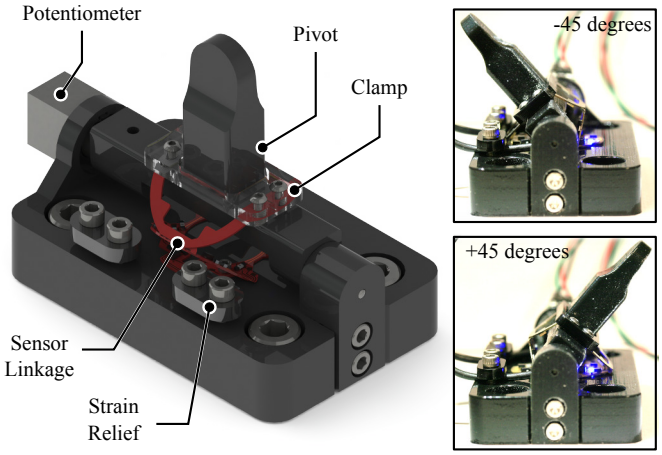

Fig. 7: Calibration setup: *(left)* rendering of calibration hardware where the sensor linkage is shown in red for clarity, *(right)* photographs of the calibration setup configuration at the extremes of travel.

V. Results and Discussion

A. Calibration

A jig was fabricated to enable calibration of the PCMEMS angle sensor linkage by coupling the kinematics of the sensor to a potentiometer which serves as ground truth. A rendering of the experimental setup is shown in Fig. 7, where insets show photographs of the jig at the extremes of travel.

As shown in our previous work [11], the performance of optoelectronic position and force sensors can be substantially improved via the inclusion of on-board temperature and environmental irradiance sensing. To this end, the to-scale sensor design includes an analog temperature sensor (MCP9700, Microchip Technology) and two environmental irradiance sensors. Although the differential configuration of the E/D pairs is quite effective at eliminating common-mode sources of noise, additional compensation can account for differences in the temperature coefficients between phototransistors as well as directional sources of ambient irradiance that may have different effects on each E/D pair. For specifics on the theory and implementation, the reader is encouraged to consult [11] as these details are left out for brevity. For convenience, we define feature space sets $\mathbf{S}_s = \{\mathbf{s}_1, \mathbf{s}_2\} \in \mathbb{R}^{N\times 2}$ where $\mathbf{s}_1, \mathbf{s}_2$ are the emitter-detector output voltages, and N is the number of data points in the time series. Additionally, let $\mathbf{S}_e = \{\mathbf{s}_t, \mathbf{s}_{e1}, \mathbf{s}_{e2}\} \in \mathbb{R}^{N\times 3}$, where $\mathbf{s}_t$ is the temperature sensor output voltage and $\mathbf{s}_{e1}, \mathbf{s}_{e2}$ are the ambient sensor output voltages. We note that $\mathbf{S}_s \cap \mathbf{S}_e = \mathbf{S} \in \mathbb{R}^{N\times 5}$ (the union of the two sets comprises a complete data set) but $\mathbf{S}_s \cup \mathbf{S}_e = \emptyset$ (E/D data and environmental data are distinct and non-interfering). We study the following feature space transformations:

- *E/D Pair Linear Mapping* $\mathbf{S}_s \to \mathbf{X}_s$: We preserve a linear mapping for E/D sensor data, i.e. for $\mathbf{s}_o \in \mathbf{S}_s$, $\mathbf{s}_o \mapsto a + b\mathbf{s}_o$.
- *Complete Data Linear Mapping* $\mathbf{S} \to \mathbf{X}$: We preserve a linear mapping for all sensor data, i.e. for $\mathbf{s}_o \in \mathbf{S}$, $\mathbf{s}_o \mapsto a + b\mathbf{s}_o$.
- *Complete Data Quadratic Mapping* $\mathbf{S} \to \Phi$: We map all sensor data to a quadratic feature space: for $\mathbf{s}_o \in \mathbf{S}$, $\mathbf{s}_o \mapsto a + b\mathbf{s}_o + c\mathbf{s}_o \odot \mathbf{s}_o$ ($\odot$ denotes element-wise multiplication).

The sensor was calibrated in this setup by sweeping the input angle over the full range of motion and recording the sensor and potentiometer outputs. The results of this calibration are shown in Fig. 8, where the left column shows the reference angle and the raw sensor outputs, and the right column shows the regression results and some error statistics. The results show that environmental compensation

This article has been accepted for publication in a future issue of this journal, but has not been fully edited. Content may change prior to final publication. Citation information: DOI 10.1109/LRA.2017.2737042, IEEE Robotics and Automation Letters

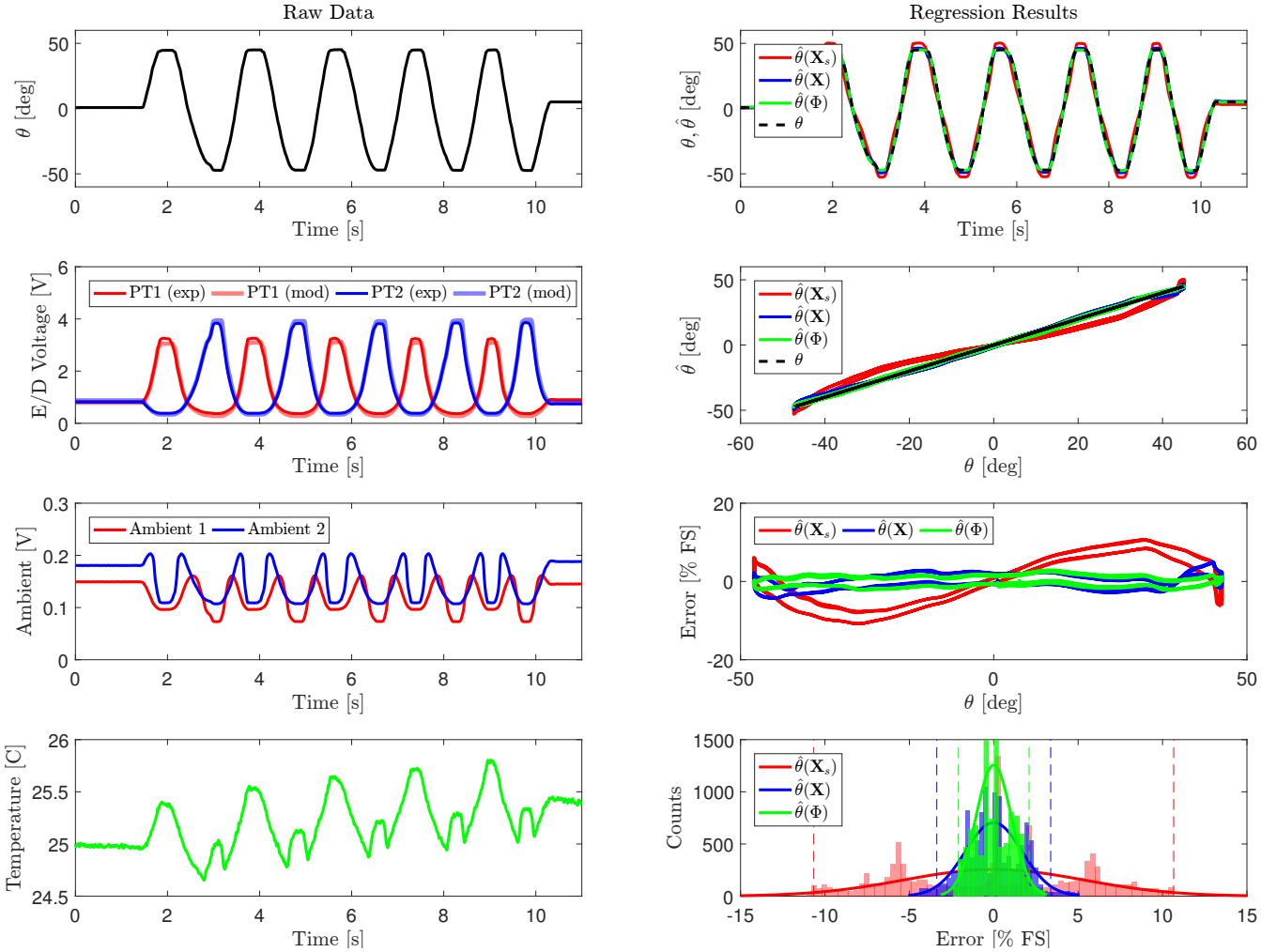

Fig. 8: Calibration results for at-scale sensor linkage in isothermal conditions: *(left, top to bottom)* input angle θ, raw emitter-detector pair outputs (model and experimental), raw ambient sensor outputs, and temperature sensor output, *(right, top to bottom)* $[\theta, \hat{\theta}(\mathbf{X}_s), \hat{\theta}(\mathbf{X}), \hat{\theta}(\Phi)]$ vs. time, $[\hat{\theta}(\mathbf{X}_s), \hat{\theta}(\mathbf{X}), \hat{\theta}(\Phi)]$ vs θ, estimation error vs. θ, and histograms showing the error distribution where dotted lines indicate 2σ.

can improve the quality of regression with a linear feature space, to the point where using a quadratic feature space only provides marginal improvements to the quality of the overall fit. The root-mean-squared error (RMSE) was found to be 0.98 degrees, or roughly 1.08% full-scale. The performance is comparable with more sophisticated and expensive shape sensing modalities (i.e. FBG) which typically boast RMS errors on the order of 2-4% full-scale [9], [14], [15]. As such, our proposed sensor performs similarly to if not better than existing approaches while providing a purely analog output, thereby obviating the need for expensive interrogation and conditioning equipment. This is paramount as we are targeting low-cost, modular, plug-and-play solutions, and as such, it is important to decouple the distal module from the proximal end both mechanically and optically which is not possible with fiber-based sensing modalities. In addition, we observe that the experimental behavior matches the analytical model at-scale (with slight deviations at the extents of travel), speaking to the generalizability and scalability of the model derived in Section II. The sensor's performance specifications are summarized in Table 1.

TABLE I: SENSOR PERFORMANCE SPECIFICATIONS

Parameter	Design Value	Actual Value	Unit
Range	±45	±45	degrees
RMSE	<2.0	0.98	degrees
Noise	<0.2	0.1	degrees
Number of Cycles	>200	>500	N/A

B. Proprioceptive Feedback in Robot-Assisted Endoscopy

The sensor linkage was attached to an endoscope-mounted robotic module to provide real-time feedback of the articulation angle for potential closed-loop feedback and trajectory execution purposes. An open-loop controller, shown schematically in Fig. 9, was designed for robot-assisted endoscopy and features a low-level PID current controller and an analog-to-PWM converter to sink current across the active SMA actuator based on a reference current profile. Low pass filters are implemented in software to filter out high frequency noise in both the current sensor and on-board proprioceptive sensor measurements. In addition, a fluid logic controller actively cools the bias actuator to enhance actuation speed. An

This article has been accepted for publication in a future issue of this journal, but has not been fully edited. Content may change prior to final publication. Citation information: DOI 10.1109/LRA.2017.2737042, IEEE Robotics and Automation Letters

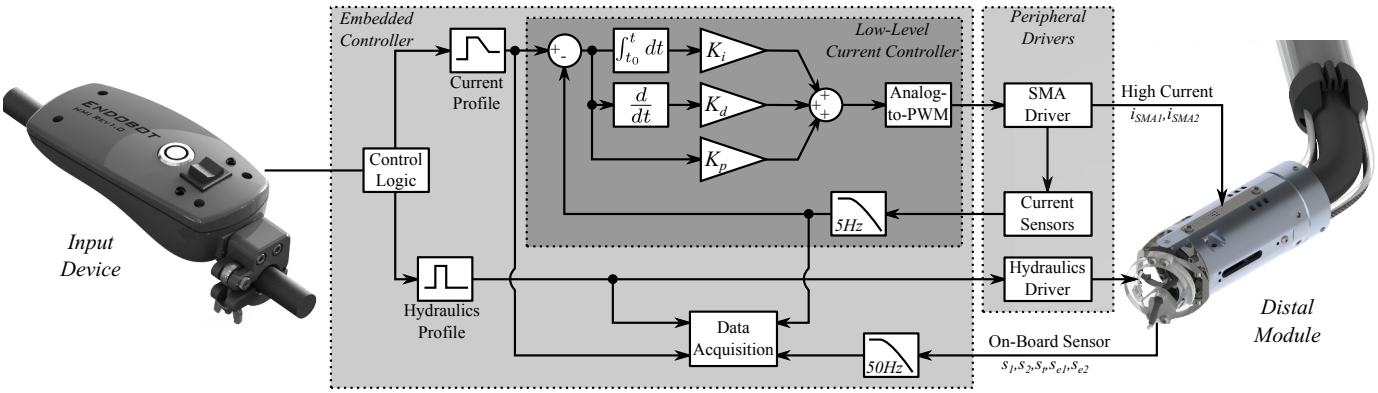

Fig. 9: Block diagram of open-loop controller (with low-level PID current loop) used to demonstrate the proprioceptive sensor's real-time feedback capabilities in a realistic application.

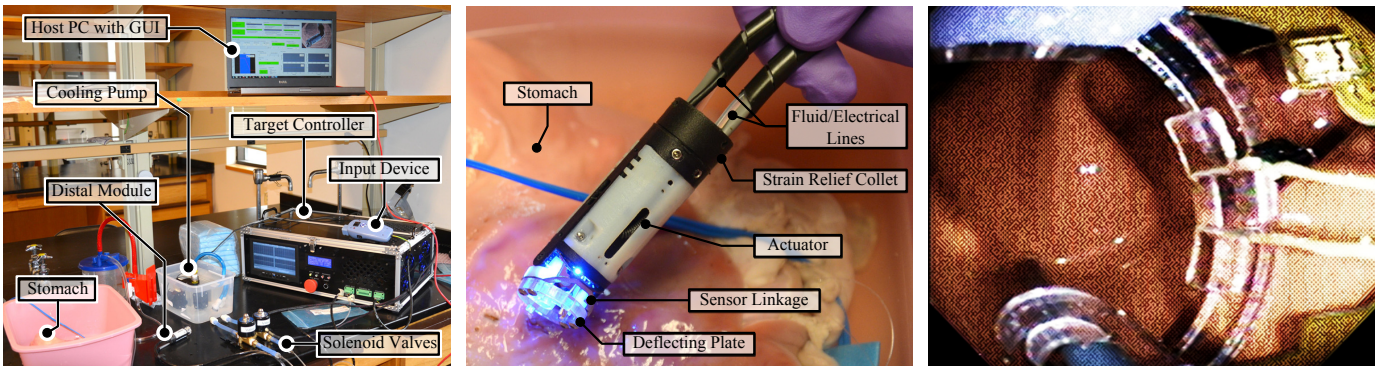

(a) (b) (c)

Fig. 10: Images of *ex vivo* test setup: *(a)* experimental setup, *(b)* close-up of a sensorized distal module in the vicinity of the porcine stomach, *(c)* module's presence in the visual field of a standard endoscope.

ergonomic, endoscope-mounted input device controls the direction of articulation. System data (desired vs. actual current profile, SMA electrical resistance, fluid logic states, and on-board sensor data) is acquired at a rate of 1 kHz. The controller is embedded on a PC104 stack consisting of an Aurora SBC (Diamond Systems) running MATLAB xPC real-time kernel, and data is acquired via a MM-32DX-AT A/D board (Diamond Systems).

1) Ex-Vivo Test with Porcine Stomach: Collaborating with endoscopists at Brigham and Women's hospital (Boston, MA), we used the sensorized module to perform a simulated ESD procedure on an excised porcine stomach. The experimental setup is shown in Fig. 10 (a). A photograph of the sensorized distal module is shown in Fig. 10 (b), as well as a representative view through the endoscope camera in Fig. 10 (c). A simulated tumor was marked on the porcine stomach, and saline fluid was injected into the submucosal space to lift the tumor off of the muscularis. The module was then used to deflect an Olympus DualKnife electrosurgical tool to create a circumferential incision around the simulated tumor margin, and system data were recorded (as shown in Fig. 11, where we use the quadratic feature space over the complete on-board sensor data set $\mathbf{S} \rightarrow \Phi$ to estimate the angle of articulation). We see a clear correlation between the applied current and the angle of articulation, indicating that the sensor is capable of providing real-time proprioceptive angle feedback. The on-board temperature sensor, in addition to providing disturbance rejection for the proprioceptive sensor, is also useful for measuring the temperature of the system as a whole. As such, a higher-level controller can use this data to monitor the system temperature in the event that the SMAs heat up the entire module near the pain threshold, thereby triggering fluid flushing to cool the system down back to an acceptable temperature. It is also important to note that electrosurgical pulses do not introduce any noise or contamination to the sensor readings. The 'jumps' at 23 seconds and 28 seconds are likely due to fluid or particulate occlusion in the emitter-detector light paths, illustrating the need for physical encapsulation and isolation of emitter-detector pairs.

VI. CONCLUSIONS AND FUTURE WORK

Herein we present a monolithically-fabricated angular proprioceptive sensor based on a flexure-based kinematic linkage and the principle of light-intensity modulation for distal implementation in endoscopic robotic systems. A complete analytical model describing the coupled kinematics and optoelectronics was derived and validated experimentally with a scaled-up model. Printed-circuit MEMS was employed to fabricate the at-scale prototype which was experimentally shown to be accurate over a range of ± 45 degrees with an

This article has been accepted for publication in a future issue of this journal, but has not been fully edited. Content may change prior to final publication. Citation information: DOI 10.1109/LRA.2017.2737042, IEEE Robotics and Automation Letters

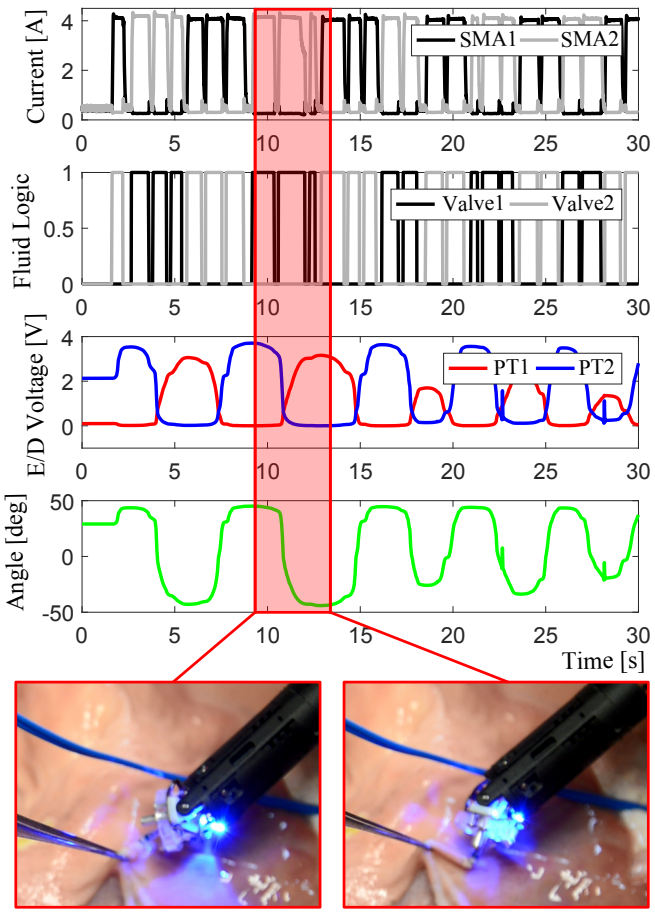

Fig. 11: Integrated system controller and sensor data: *(from top)* current commands sent to each SMA, logic-level signals sent to fluid cooling solenoid valves, emitter-detector pair output voltages, and estimated angle $\hat{\theta}(\Phi)$. Insets show photographs of the module during the incision process.

RMSE of 0.98 degrees. As a practical demonstration, the sensor linkage was attached to a distal robotic module and was used during a simulated *ex vivo* ESD procedure. An open-loop controller was implemented to control the deflection of a flexible electrosurgical tool, and the sensor demonstrated real-time angular feedback.

Future work will focus on the integration of encapsulating structures to protect the exposed emitter-detector pairs from fluid and detritus that may be present during the procedure. While blood is uncommon during ESD as the procedure is mostly superficial, water, saline, and GI fluid could potentially block the light paths between emitter-detector pairs, thereby compromising their operation. While sensor redundancy does present some robustness in the event that an emitter-detector pair gets blocked by fluid or debris, it is desirable to pursue mechanical encapsulating solutions to isolate the emitter-detector pairs from the environment. Leveraging recent work in combining PCMEMS manufacturing with soft elastomeric materials [16], the sensing linkage presented in this paper will be encapsulated in a silicone bellows that will physically isolate the emitter-detector pairs without restricting motion of the articulating mechanisms. We will work to further reduce the field-of-view occlusion towards the aim of device transparency when not in use. We will also focus on the development of controllers that will leverage on-board sensor feedback to control on-board actuation, thereby demonstrating fully-distal loop closure in an endoscope-based robot for both teleoperation and low-level task automation in endoscopic procedures, specifically ESD. In addition, we are working closely with clinical collaborators to develop an appropriate *in vivo* animal study in a porcine model to demonstrate device robustness and utility in a clinically realistic environment.

REFERENCES

[1] K. Taniguchi, A. Nishikawa, and M. Sekimoto, "Classification, design and evaluation of endoscope robots," *Robot Surgery*, vol. 1, no. January, p. 172, 2010.

[2] K.-y. Ho, S. J. Phee, A. Shabbir, S. C. Low, V. A. Huynh, A. P. Kencana, K. Yang, D. Lomanto, B. Y. J. So, Y. Y. J. Wong, and S. C. S. Chung, "Endoscopic submucosal dissection of gastric lesions by using a Master and Slave Transluminal Endoscopic Robot (MASTER).," *Gastrointestinal endoscopy*, vol. 72, no. 3, pp. 593–9, 2010.

[3] G. P. Mylonas, V. Vitiello, T. P. Cundy, A. Darzi, and G.-z. Yang, "CYCLOPS : A Versatile Robotic Tool for Bimanual Single-Access and Natural-Orifice Endoscopic Surgery," *IEEE International Conference on Robotics and Automation*, pp. 2436–2442, 2014.

[4] J. Ruiter, E. Rozeboom, M. Van Der Voort, M. Bonnema, and I. Broeders, "Design and evaluation of robotic steering of a flexible endoscope," *Proceedings of the IEEE RAS and EMBS International Conference on Biomedical Robotics and Biomechatronics*, pp. 761–767, 2012.

[5] M. F. Traeger, D. B. Roppenecker, M. R. Leininger, F. Schnoes, and T. C. Lueth, "Design of a spine-inspired kinematic for the guidance of flexible instruments in minimally invasive surgery," *2014 IEEE/RSJ International Conference on Intelligent Robots and Systems*, no. Iros, pp. 1322–1327, 2014.

[6] B. P. M. Yeung and P. W. Y. Chiu, "Application of robotics in gastrointestinal endoscopy: A review," *World Journal of Gastroenterology*, vol. 22, no. 5, pp. 1811–1825, 2016.

[7] J. Gafford, R. Wood, and C. Walsh, "A High-Force, High-Stroke Distal Robotic Add-On for Endoscopy," *2017 IEEE International Conference on Robotics and Automation (ICRA)*, 2017.

[8] Y. Chen, J. M. Oliveira, and I. W. Hunter, "Two-axis bend sensor design, kinematics and control for a continuum robotic endoscope," in *Proceedings - IEEE International Conference on Robotics and Automation*, pp. 704–710, 2013.

[9] S. C. Ryu and P. E. Dupont, "FBG-based shape sensing tubes for continuum robots," *Proceedings - IEEE International Conference on Robotics and Automation*, pp. 3531–3537, 2014.

[10] C. Shi, X. Luo, P. Qi, T. Li, S. Song, Z. Najdovski, H. Ren, and T. Fukuda, "Shape Sensing Techniques for Continuum Robots in Minimally Invasive Surgery: A Survey," *IEEE Transactions on Biomedical Engineering*, vol. 9294, no. c, pp. 1–1, 2016.

[11] J. Gafford, F. Doshi-Velez, R. Wood, and C. Walsh, "Machine learning approaches to environmental disturbance rejection in multi-axis opto-electronic force sensors," *Sensors and Actuators A: Physical*, vol. 248, pp. 78–87, 2016.

[12] J. B. Gafford, R. J. Wood, and C. J. Walsh, "Self-Assembling, Low-Cost, and Modular mm-Scale Force Sensor," *IEEE Sensors Journal*, vol. 16, no. 1, pp. 69–76, 2016.

[13] J. Gafford, T. Ranzani, S. Russo, A. Degirmenci, S. Kesner, R. D. Howe, R. J. Wood, and C. Walsh, "Towards Medical Devices with Integrated Mechanisms, Sensors and Actuators via Printed-Circuit MEMS," *Journal of Medical Devices*, vol. 11, no. March, 2016.

[14] H. Liu, A. Farvardin, S. A. Pedram, I. Iordachita, R. H. Taylor, and M. Armand, "Large deflection shape sensing of a continuum manipulator for minimally-invasive surgery," in *2015 IEEE International Conference on Robotics and Automation (ICRA)*, pp. 201–206, May 2015.

[15] S. Sefati, F. Alambeigi, I. Iordachita, M. Armand, R. J. Murphy, and M. Armand, "Fbg-based large deflection shape sensing of a continuum manipulator: Manufacturing optimization," in *2016 IEEE SENSORS*, pp. 1–3, Oct 2016.

[16] S. Russo, T. Ranzani, J. Gafford, C. J. Walsh, and R. J. Wood, "Soft pop-up mechanisms for micro surgical tools: Design and characterization of compliant millimeter-scale articulated structures," in *2016 IEEE International Conference on Robotics and Automation (ICRA)*, pp. 750–757, May 2016.